A coupled finite element–element-free Galerkin method

T. Belytschko, D. Organ, Y. Krongauz

Abstract A procedure is developed for coupling meshless methods such as the element-free Galerkin method with finite element methods. The coupling is developed so that continuity and consistency are preserved on the interface elements. Results are presented for both elastostatic and elastodynamic problems, including a problem with crack growth.

1
Introduction

Meshless methods, such as the element-free Galerkin (EFG) method [Belytschko, Lu, and Gu (1994), Belytschko, Lu, Gu, and Tabbara (1995)], offer considerable potential simplifications for many problems, particularly those associated with the growth of surfaces, such as in crack propagation. In arbitrary crack growth problems, for instance, finite element (FE) methods entail remeshing in each step of the evolution of the crack. While the rapid recent development of automatic mesh generators has made this less burdensome, for nonlinear problems and dynamic crack growth, methods based on remeshing are quite unattractive because of the projections of field variables which are needed and the many logistical problems which must be dealt with in such approaches. When the crack moves along element edges, various node releasing methods and moving element methods as described by Nishioka and Atluri (1986) can be used.

Nevertheless the maturity and comprehensive capabilities of finite element packages are very difficult to duplicate, and it is often desirable to use meshless methods only in the subdomains where their unique advantages are beneficial. Thus, in modeling crack growth in a complicated engineering structure with stiffeners and complex interconnections, it would be desirable to have the versatility of the meshless methods such as EFG in the areas of crack growth, but rely on the comprehensive capabilities of a finite element software package in the remainder of the domain. Furthermore, because of its versatility, EFG requires markedly more computer resources.

Thus, limiting EFG modeling to the areas where it is needed can save computer time.

In this paper, a methodology for coupling EFG to finite element methods for continuum problems is presented. This method employs interface elements, within which the shape functions are comprised of the EFG and FE shape functions. It is shown that the resulting functions satisfy consistency, which insures convergence of the method; consistency is also verified by showing that the patch test is satisfied for irregular meshes. In elastostatic problems, the method retains the rate of convergence of the finite element method for the domain; the higher rates of convergence of EFG can not be reproduced because the errors from the finite elements dominate. The method is applicable both to EFG and to other meshless methods, such as smooth particle hydrodynamics (SPH) and wavelet-based methods.

Since the methodology is intended for problems of dynamic fracture, we have also included an example involving dynamic fracture. The method is shown to reproduce the results obtained by a model based entirely on EFG quite well, yet reduce computation time by a factor of 2.

The method is illustrated in the context of elastostatics and elastodynamics. The outline of the paper is as follows. Section 2 reviews the basic equations of elastostatics and elastodynamics. Section 3 presents the EFG shape functions and the shape functions for the coupling; consistency is also proved. Examples are given in Sect. 5, followed by a discussion and conclusions in Sect. 6.

2
Basic equations

2.1
Elastostatics

We consider small displacement elastostatics, which is governed by the equations of equilibrium:

$$\nabla \cdot \sigma + \mathbf{b} = 0 \quad \text{in } \Omega, \tag{2.1}$$

where

$$\sigma = \mathbf{D}\varepsilon \quad \text{and} \quad \varepsilon = \nabla_s \mathbf{u}.$$

In the above, Ω is the domain of the body, σ is the stress tensor, ε is the strain, $\mathbf{b}$ is the body force per unit volume, $\mathbf{D}$ is a matrix of material moduli, $\mathbf{u}$ is the displacement, $\nabla \cdot$ is the divergence operator, and ∇_s is the symmetric gradient operator.

T. Belytschko, D. Organ, Y. Krongauz
Department of Civil Engineering, Robert R. McCormick School of Engineering and Applied Science, The Technological Institute, Northwestern University, Evanston, IL 60208-3109, USA.

Correspondence to: T. Belytschko

The boundary conditions are

(essential b.c.) $u_i = \bar{u}_i$ on Γ_{u_i},   (2.2a)

(natural b.c.) $\sigma_{ij} n_j = \bar{t}_i$ on Γ_{t_i},   (2.2b)

where Γ is the domain boundary, and $\bar{u}_i$ and $\bar{t}_i$ are prescribed boundary displacements and tractions, respectively.

The weak form is

$$\int_\Omega \delta\varepsilon : \sigma d\Omega = \sum_{i-1}^{n_{sd}} \int_{\Gamma_{t_i}} \delta u_i \bar{t}_i d\Gamma + \int_\Omega \delta u \cdot b d\Omega,   (2.3)$$

where $\delta\varepsilon = \nabla_s(\delta u)$.

2.2
Elastodynamics
The strong form of the initial/boundary value problem for small displacement elastodynamics is as follows:

$$\nabla \cdot \sigma + b = \rho \ddot{u}   \text{in } \Omega,   (2.4)$$

with the auxiliary conditions:

(essential b.c.) $u_i = \bar{u}_i$ on Γ_{u_i},   (2.5a)

(natural b.c.) $\sigma_{ij} n_j = \bar{t}_i$ on Γ_{t_i},   (2.5b)

(displacement i.c.) $u(x,0) = u_0(x)$ $x \in \Omega$,   (2.5c)

(velocity i.c.) $\dot{u}(x,0) = v_0(x)$ $x \in \Omega$,   (2.5d)

where ρ is the mass density, $\ddot{u}$ signifies two time derivatives, and u_0 and v_0 are initial displacements and velocities, respectively.

The weak form is

$$\int_\Omega \rho \delta u \cdot \ddot{u} d\Omega + \int_\Omega \delta\varepsilon : \sigma d\Omega = \sum_{i=1}^{n_{sd}} \int_{\Gamma_{t_i}} \delta u_i \bar{t}_i d\Gamma + \int_\Omega \delta u \cdot b d\Omega.   (2.6)$$

The weak forms in (2.3) and (2.6) are used in the Galerkin procedure to develop the discrete equations. Since both FE and EFG are discretized by Galerkin approximations, the weak forms can be used directly in the coupled method without any modifications.

3
Coupling procedure
The coupling between finite elements and EFG is accomplished by introducing interface elements between the FE and EFG domains (see Fig. 1). In these interface elements, a hybrid displacement approximation is defined that satisfies displacement continuity across the interface boundaries. Before these interface elements are described in detail, the separate FE and EFG displacement approximations will be defined.

3.1
Shape functions
Both FE and EFG use similar forms in approximating the displacements in the Galerkin procedure:

$$u_i^h(x,t) = \sum_{I=1}^{n} \bar{N}_I(x) u_{iI}(t),   (3.1)$$
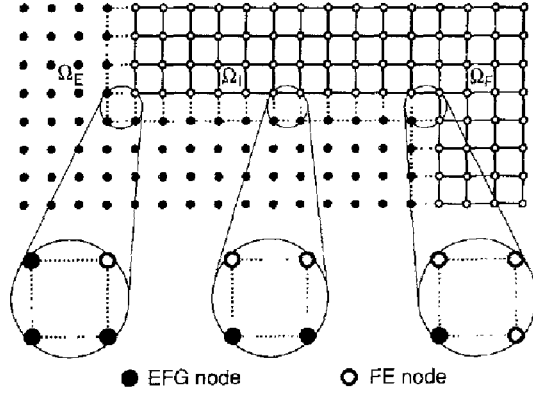

● EFG node   O FE node

Fig. 1. Subdomains used for FE-EFG coupling. The coupling formulation can accommodate any combination of EFG nodes and FE nodes associated with an interface element

187

where $\bar{N}_I$ are shape functions that depend on the method and u_{iI} are nodal coefficients for displacement component i at node I.

The specific shape functions for FE and EFG will be defined assuming two dimensional analysis of elastodynamics. Reduction to one dimension is trivial, and expansion to higher dimensions is also straightforward. For elastostatics, the time dependence should be eliminated from the equations.

3.1.1
FE shape functions
The interpolation function for the displacement u_i in an isoparametric element is (see Hughes (1987))

$$u_i^h(x,t) = \sum_{I=1}^{n_{en}} N_I(\xi(x)) u_{iI}(t),   x \in \Omega_F^e,   (3.2)$$

where n_{en} is the number of element nodes. For the 4-node element used here, N_I are the standard bilinear shape functions:

$$N_I(\xi) = \tfrac{1}{4}(1 + \xi_I \xi)(1 + \eta_I \eta).   (3.3)$$

In the above expressions, $\xi(x) = (\xi(x), \eta(x))$ is a mapping from the physical domain to the parent domain (only the inverse mapping is usually defined), and (ξ_I, η_I) are the nodal coordinates in the parent domain ($\xi \in [-1,1], \eta \in [-1,1]$).

3.1.2
EFG shape functions
In the EFG method, the displacement is approximated by moving least-squares approximations (MLS) (see Lancaster and Salkauskas (1981)). The MLS approximation $u_i^h(x,t)$ is given by

$$u_i^h(x,t) = \sum_{j=1}^{m} p_j(x) a_{ij}(x,t) \equiv p^T(x) a_i(x,t),   (3.4)$$

where $p(x)$ is a complete polynomial basis of arbitrary order and $a_i(x,t)$ are coefficients which are functions of the space coordinates x and time t. We have used a linear basis in two dimensions:

$$p^T(x) = [1,x,y];   m = 3.$$

The coefficients $a_i(\mathbf{x},t)$ in (3.4) are obtained at any point $\mathbf{x}$ by minimizing the following:

$$S = \sum_{l=1}^{n_{sn}} w(\mathbf{x} - \mathbf{x}_l)[u_{tl}(t) - \mathbf{p}^T(\mathbf{x}_l)\mathbf{a}_i(\mathbf{x},t)]^2, \qquad (3.5)$$

where n_{sn} is the number of nodes in the support or domain of influence of $\mathbf{x}$ for which the weight function $w(\mathbf{x} - \mathbf{x}_l) \neq 0$, and u_{tl} is the coefficient associated with node l at $\mathbf{x}_l$.

The stationary value of S in (3.5) with respect to $a_i(\mathbf{x},t)$ leads to

$$\mathbf{a}_i(\mathbf{x},t) = \mathbf{A}^{-1}(\mathbf{x})\mathbf{C}(\mathbf{x})\mathbf{u}_i(t), \qquad (3.6)$$

where

$$\mathbf{A}(\mathbf{x}) = \sum_{l=1}^{n_{sn}} w(\mathbf{x} - \mathbf{x}_l)\mathbf{p}(\mathbf{x}_l)\mathbf{p}^T(\mathbf{x}_l), \qquad (3.7a)$$

$$\mathbf{C}(\mathbf{x}) = [w(\mathbf{x} - \mathbf{x}_1)\mathbf{p}(\mathbf{x}_1), w(\mathbf{x} - \mathbf{x}_2)\mathbf{p}(\mathbf{x}_2),\dots,w(\mathbf{x} - \mathbf{x}_n)\mathbf{p}(\mathbf{x}_n)], \qquad (3.7b)$$

$$\mathbf{u}_i^T(t) = [u_{t1}(t), u_{t2}(t),\dots,u_{tn}(t)]. \qquad (3.7c)$$

By substituting (3.6) into (3.4), the MLS approximants are defined in a form similar to (3.1):

$$u_i^h(\mathbf{x},t) = \sum_{l=1}^{n_{sn}} \phi_l(\mathbf{x})u_{tl}(t), \quad \mathbf{x} \in \Omega_E, \qquad (3.8)$$

where the EFG shape functions are defined as

$$\phi_l(\mathbf{x}) = \sum_{j=1}^{m} p_j(\mathbf{x})(\mathbf{A}^{-1}(\mathbf{x})\mathbf{C}(\mathbf{x}))_{jl}. \qquad (3.9)$$

EFG approximants *do not* satisfy the Kronecker delta criterion: $\phi_l(\mathbf{x}_j) \neq \delta_{lj}$. Consequently, the imposition of essential boundary conditions is more complicated than for the standard FEM. Several methods have been developed, including Lagrange multipliers [Belytschko, Lu, and Gu (1994)], modified variational principles [Lu, Belytschko, and Gu (1994)], and for explicit dynamics, collocation at nodes on the essential boundaries [Belytschko and Tabbara (to appear)]. Note that in the coupled method, this can be avoided if the essential boundaries are along FE domains, where the essential boundary conditions can be prescribed directly.

The weight function $w(\mathbf{x} - \mathbf{x}_l)$ in (3.7a) and (3.7b) is a monotonically decreasing function of $\|\mathbf{x} - \mathbf{x}_l\|$, and its continuity is equal to the continuity of the shape functions (3.9) [Lancaster and Salkauskas (1981)]. Defining $d_l = \|\mathbf{x} - \mathbf{x}_l\|$, and $r = d_l/d_{m_l}$, where d_{m_l} is the radius of the support of the Ith node, the weight can be written more compactly as a function of the normalized distance r. Some examples of weight functions are:

- Gaussian:

$$w(r) = \begin{cases} e^{-(r/0.4)^2} & \text{for } r \leq 1, \\ 0 & \text{for } r > 1 \text{ or across boundaries.} \end{cases} \qquad (3.10a)$$

- cubic spline:

$$w(r) = \begin{cases} \frac{2}{3} - 4r^2 + 4r^3 & \text{for } r \leq \frac{1}{2}, \\ \frac{4}{3} - 4r + 4r^2 - \frac{4}{3}r^3 & \text{for } \frac{1}{2} < r \leq 1, \\ 0 & \text{for } r > 1 \text{ or across boundaries.} \end{cases} \qquad (3.10b)$$

- quartic polynomial:

$$w(r) = \begin{cases} 1 - 6r^2 + 8r^3 - 3r^4 & \text{for } r \leq 1, \\ 0 & \text{for } r > 1 \text{ or across boundaries.} \end{cases} \qquad (3.10c)$$

The support radius or domain of influence at a node, d_{m_l}, is computed by

$$d_{m_l} = d_{max}c_l, \qquad (3.11)$$

where d_{max} is a scaling factor. The distance c_l is determined by searching for enough adjacent nodes to satisfy the basis. The multiplier d_{max} is typically 2.0–4.0 for static analyses and 2.0–2.5 for dynamics.

Note that the weight function becomes a function of time in dynamic fracture problems since as a crack propagates, the boundaries and domains of influence d_{m_l} change. In these cases, $\mathbf{A}(\mathbf{x},t)$, $\mathbf{C}(\mathbf{x},t)$, and the resulting shape functions $\phi_l(\mathbf{x},t)$ are time dependent. The time dependence has not been explicitly included in the above expressions, since it applies only to dynamic fracture problems and only affects points in a region near a propagating crack tip.

3.2
Interface displacement approximation

To illustrate the coupling procedure, again consider the domain in Fig. 1 with additional detail shown in Fig. 2. In Ω_E, the displacement at a point is approximated using the MLS approximants in (3.8), and in Ω_F, the finite element interpolants in (3.2) are employed in each element subdomain Ω_F^e. In Ω_I, the interface region, the following expression is used:

$$u_i^h(\mathbf{x},t) = u_i^{FE}(\mathbf{x},t) + R(\mathbf{x})[u_i^{EFG}(\mathbf{x},t) - u_i^{FE}(\mathbf{x},t)]$$

$$= [1 - R(\mathbf{x})]u_i^{FE}(\mathbf{x},t) + R(\mathbf{x})u_i^{EFG}(\mathbf{x},t), \quad \mathbf{x} \in \Omega_I, \quad (3.12)$$

where u_i^{FE} and u_i^{EFG} are approximations for u_i in Ω_I given by the FE and EFG approximations, respectively, and $R(\mathbf{x})$ is a ramp function similar to that defined by Lu, Belytschko, and Liu (1991) and Belytschko, Chang, and Lu (1989) for coupling finite elements and boundary elements. $R(\mathbf{x})$ is defined using the finite element shape functions in (3.3):

$$R(\mathbf{x}) = \sum_{\substack{J \\ x_J \in \Gamma_F}} N_J(\mathbf{x}). \qquad (3.13)$$

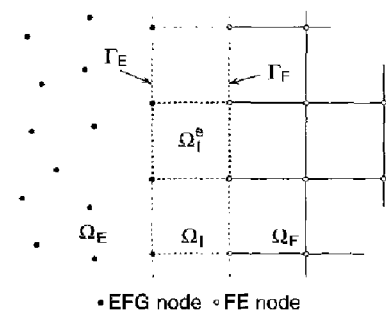$\bullet$ EFG node $\circ$ FE node

Fig. 2. Interface element used for FE-EFG coupling

In words, the ramp function is equal to the sum of the FE shape functions associated with interface element nodes that are on the EFG boundary; $R(\mathbf{x})$ is shown for different configurations in Fig. 3. Note that

$$R(\mathbf{x}) = \begin{cases} 1 & \mathbf{x} \in \Gamma_E, \\ 0 & \mathbf{x} \in \Gamma_F, \end{cases}$$

and it varies linearly along interface element boundaries adjacent to other interface elements. Therefore, the approximation (3.12) reduces to u_i^{EFG} (3.8) on Γ_E and u_i^{FE} (3.2) on Γ_F, ensuring continuity.

The interface shape functions can be developed by substituting the displacement approximations (3.2) and (3.8)

into (3.12):

$$u_i^h(\mathbf{x},t) = [1 - R(\mathbf{x})] \sum_{I=1}^{n_{en}} N_I(\boldsymbol{\xi}(\mathbf{x})) u_{iI}(t) + R(\mathbf{x}) \sum_I \phi_I(\mathbf{x}) u_{iI}(t)$$

$$\equiv \sum_{I=1}^{n_{sn}} \tilde{N}_I(\mathbf{x}) u_{iI}(t), \quad \mathbf{x} \in \Omega_I^e, \qquad (3.14)$$

where the interface shape functions $\tilde{N}_I(\mathbf{x})$ are

$$\tilde{N}_I(\mathbf{x}) = \begin{cases} [1 - R(\mathbf{x})]N_I(\boldsymbol{\xi}(\mathbf{x})) + R(\mathbf{x})\phi_I(\mathbf{x}) & \mathbf{x}_I \in \Omega_I^e, \quad (3.15a) \\ R(\mathbf{x})\phi_I(\mathbf{x}) & \mathbf{x}_I \notin \Omega_I^e. \quad (3.15b) \end{cases}$$

(3.15a) applies to the shape functions associated with the interface element nodes and (3.15b) applies to shape functions associated with nodes outside the particular interface element. The interface shape function derivatives are:

$$\tilde{N}_{I,i} = \begin{cases} R_{,i}N_I + [1 - R]N_{I,i} + R_{,i}\phi_I + R\phi_{I,i} & \mathbf{x}_I \in \Omega_I^e, \\ R_{,i}\phi_I + R\phi_{I,i} & \mathbf{x}_I \notin \Omega_I^e, \end{cases} \quad (3.16)$$

where

$$R_{,i} = \sum_{\substack{J \\ \mathbf{x}_J \in \Gamma_E}} N_{J,i}.$$

Typical interface shape functions are shown in one dimension in Fig. 4 and in two dimensions in Fig. 5. Note that the derivatives are discontinuous along Γ_E and Γ_F as well as along
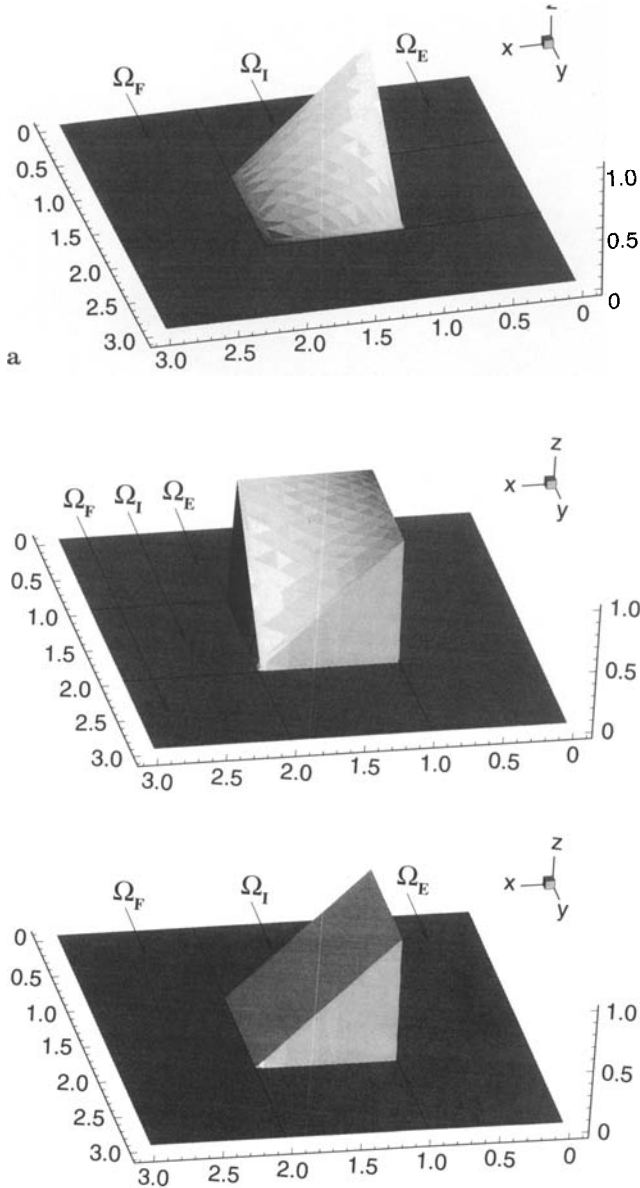

Fig. 3a–c. Sample ramp functions, $R(\mathbf{x})$, for the three interface elements shows in Fig. 1. $R(\mathbf{x})$ is only shown for one interface element in each plot. **a** One DFG node, three FE nodes. **b** Three EFG nodes, one FE node. **c** Two nodes, two FE nodes
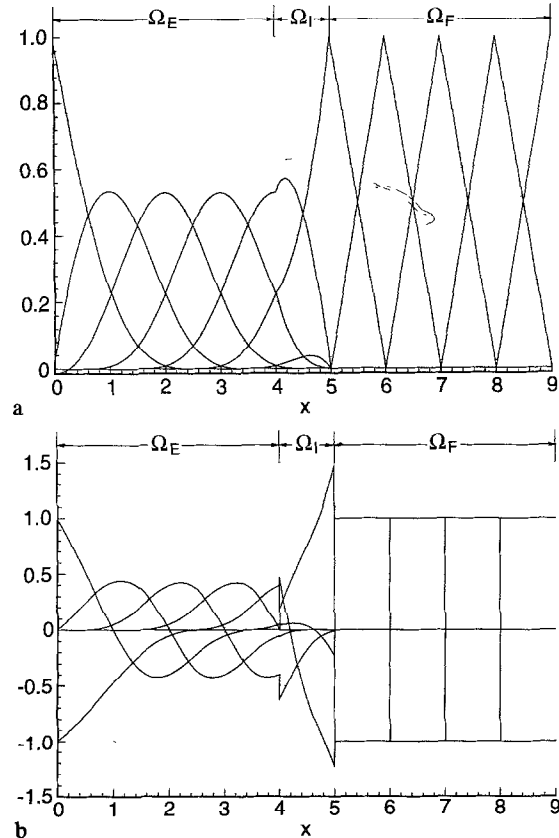

Fig. 4a–b. Interface shape functions in one dimension using the cubic spline weight function in (3.10b) with $d_{max} = 2.5$. **a** Shape function, $\bar{N}(x)$. **b** Shape function derivatives, $\bar{N}_{,x}(x)$
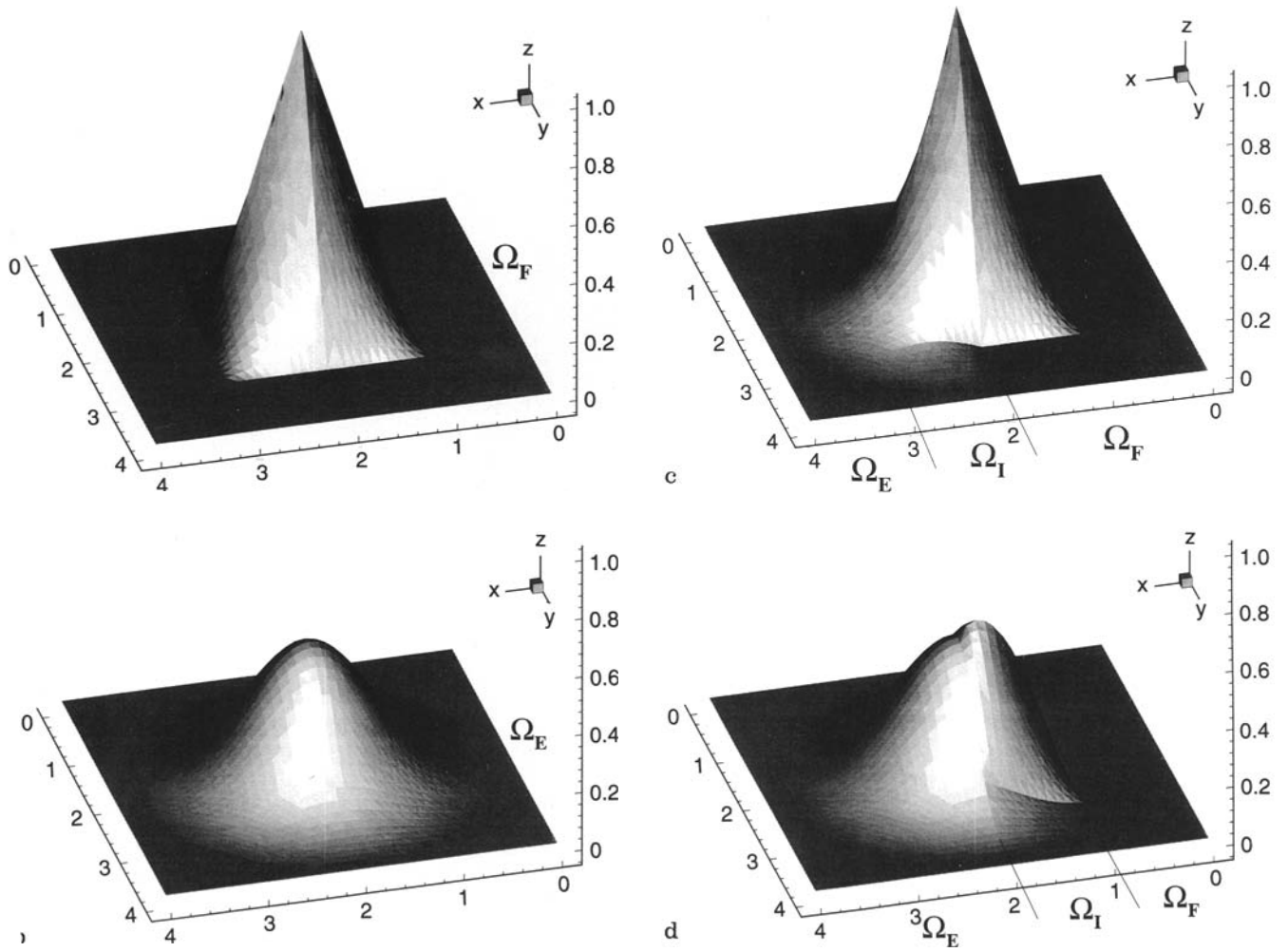
Fig. 5a–d. Interface shape functions in two dimensions using the cubic spline weight function in (3.10b) with $d_{max} = 2.0$. a Standard FE shape function. b Standard EFG shape function. c Shape function for a node on Γ_I. d Shape function for a node on Γ_E

interior interface element boundaries. These discontinuities do not adversely affect the overall results since they only affect a small number of nodes.

Both the FE interpolants and the EFG approximants (when the basis $p(x)$ is linear or higher order) satisfy consistency; i.e., if the nodal coefficients are given by a linear field, $u_{il} = c_{ij}x_{jl}$, then the approximation reproduces a linear field, $u_i = c_{ij}x_j$. (Some authors define this as completeness; see Hughes (1987).) For FE, this property follows directly from the isoparametric concept [Hughes (1987)]. In EFG, the MLS approximants can exactly represent any linear combination of the basis functions [Lancaster and Salkauskas (1986)]. In terms of the shape functions, the property is

$$\sum_{I}^{n_{en}} N_I(x)x_{jI} = \sum_{I}^{n_{sn}} \phi_I(x)x_{jI} \equiv x_j. \qquad (3.17)$$

The interface approximation must also satisfy consistency. To show this, consider the expression in (3.14) with the nodal coefficients given as $u_{il} = c_{ij}x_{jl}$ repeated indices are summed. Then,

$$u_i^h = [1 - R]\sum_{I=1}^{n_{en}} N_I(c_{ij}x_{jl}) + R\sum_{I=1}^{n_{sn}} \phi_I(c_{ij}x_{jl})$$

$$= [1 - R]c_{ij}\underbrace{\sum_{I=1}^{n_{en}} N_I x_{jl}}_{\substack{x_j \\ \text{by (5.17)}}} + R c_{ij}\underbrace{\sum_{I=1}^{n_{sn}} \phi_I x_{jl}}_{\substack{x_j \\ \text{by (3.17)}}}$$

$$= [1 - R]c_{ij}x_j + R c_{ij}x_j$$

$$= c_{ij}x_j.$$

Consequently, the interface approximation can exactly represent linear fields. This property is also established by a patch test in Sect. 5.

4
Discrete equations

4.1
Elastostatics

In the variational form of equilibrium (2.3), approximate u and δu by

$$u^h(x) = \sum_I \bar{N}_I(x)d_I \quad \text{and} \quad \delta u^h(x) = \sum_I \bar{N}_I(x)\delta d_I,$$

where

$$\bar{N}_I(\mathbf{x}) = \begin{cases} N_I(\xi(\mathbf{x})) & \mathbf{x} \in \Omega_F^e \quad \text{(from (3.3))}, \\ \phi_I(\mathbf{x}) & \mathbf{x} \in \Omega_E \quad \text{(from (3.9))}, \\ \tilde{N}_I(\mathbf{x}) & \mathbf{x} \in \Omega_I^e \quad \text{(from (3.15))}. \end{cases} \quad (4.1)$$

The nodal test function values $\delta\mathbf{d}_I$ are arbitrary, except on Γ_u, resulting in:

$$\mathbf{K}\mathbf{d} = \mathbf{f}^{\text{ext}}, \quad (4.2)$$

where

$$\mathbf{K}_{IJ} = \int_\Omega \mathbf{B}_I^T \mathbf{D} \mathbf{B}_J \, d\Omega, \quad \text{and} \quad \mathbf{f}_I^{\text{ext}} = \int_{\Gamma_t} \bar{N}_I \bar{\mathbf{t}} \, d\Gamma + \int_\Omega \bar{N}_I \mathbf{b} \, d\Omega. \quad (4.3)$$

In the above, $\mathbf{B}_I$ is a matrix of shape function derivatives: $\mathbf{B}_{II} = \partial\bar{N}_I/\partial x_i$. In contrast to Nayroles, Touzot, and Villon (1992), the derivatives of $\mathbf{a}(\mathbf{x}, t)$ are included in computing the shape function derivatives in $\mathbf{B}_I$ [Belytschko, Lu, and Gu (1994)].

4.2
Elastodynamics
For the weak form of the equations of motion in (2.6), set

$$\mathbf{u}^h(\mathbf{x}, t) = \sum_I \bar{N}_I(\mathbf{x}) \mathbf{d}_I(t) \quad \text{and} \quad \delta\mathbf{u}^h(\mathbf{x}) = \sum_I \bar{N}_I(\mathbf{x}) \delta\mathbf{d}_I.$$

where $\bar{N}_I$ is given by (4.1). Again, the nodal test function values $\delta\mathbf{d}_I$ are arbitrary, resulting in the matrix form:

$$\mathbf{M}\ddot{\mathbf{d}} + \mathbf{f}^{\text{int}} = \mathbf{f}^{\text{ext}}, \quad (4.4)$$

where

$$M_{IJ} = \sum_J \int_\Omega \rho \bar{N}_I, \bar{N}_J \, d\Omega, \quad \mathbf{f}_I^{\text{int}} = \int_\Omega \mathbf{B}_I^T \sigma d\Omega, \quad \mathbf{f}_I^{\text{ext}} = \int_{\Gamma_t} \bar{N}_I \bar{\mathbf{t}} \, d\Gamma$$

$$+ \int_\Omega \bar{N}_I \mathbf{b} \, d\Omega. \quad (4.5)$$

The mass matrix in (4.5) has been diagonalized by the row-sum technique and the time dependence of the shape functions (in fracture problems where the boundaries are changing) has been neglected in the mass matrix.

5
Numerical examples

5.1
Elastostatics
The system of equations in (4.2) is solved numerically by standard LU decomposition. The integrals in (4.3) are evaluated by numerical quadrature using elements in Ω_F and Ω_I and a cell structure that overlays Ω_E. The quartic polynomial weight function in (3.10c) was used for the EFG shape functions, and the domain of influence multiplier, d_{max}, was set to 2.0, unless otherwise indicated.

5.1.1
Patch test
Both regular and irregular meshes, shown in Fig. 6, were used in patch tests. The patch test was done with the displacement field

$$\mathbf{u}(\mathbf{x}) = \begin{Bmatrix} x \\ y \end{Bmatrix} \quad (5.1)$$

applied at the boundary. The exact solution is given by (5.1) in the absence of body forces. The coupled FE-EFG formulation passed the test for both kinds of meshes. "Passed" here means that the linear field was reproduced to within roundoff and quadrature errors; using double precision on an HP9000/700 workstation, the maximum error in the displacement was of order 10^{-6}.

5.1.2
Cantilever beam
The solution for a cantilever beam subject to an end load as shown in Fig. 7 is given by Timoshenko and Goodier (1970) as

$$u_x = \frac{-Py}{6EI}\left[(6L - 3x)x + (2 + v)\left(y^2 - \frac{D^2}{4}\right)\right], \quad (5.2a)$$

$$u_y = \frac{P}{6EI}\left[3vy^2(L - x) + (4 + 5v)\frac{D^2x}{4} + (3L - x)x^2\right]. \quad (5.2b)$$
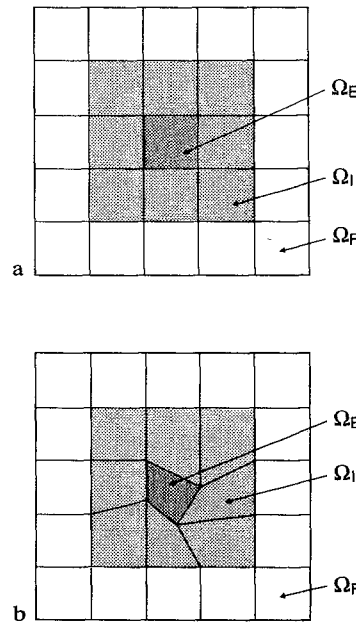

Fig. 6a,b. Patch test meshes. a Regular mesh. b Irregular mesh
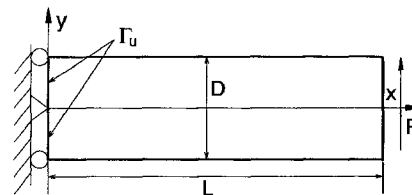

Fig. 7. Cantilever beam for comparison to the analytic solution from Timoshenko and Goodier (1970)

The stresses are given by

$$\sigma_{xx} = \frac{-P(L-x)y}{I},$$ (5.3a)

$$\sigma_{yy} = 0,$$ (5.3b)

$$\sigma_{xy} = \frac{P}{2I}\left(\frac{D^2}{4} - y^2\right),$$ (5.3c)

where I is the moment of inertia and for a beam with rectangular cross-section and unit thickness:

$$I = \frac{D^3}{12}.$$

The displacements (5.2a) and (5.2b) are prescribed as essential boundary conditions at $x = 0$, $-D/2 \le y \le D/2$; the remaining boundaries are traction boundaries. For the discrete model, the left half of the beam was modeled by finite elements (Ω_F) and right half by EFG (Ω_E), so that the essential boundary conditions could be imposed easily. The following parameters were used for the numerical simulation: $E = 1000$, $\nu = 0.3$, $D = 1$, and $L = 8$. Regular meshes were used, with 4×4 quadrature in each element or EFG cell. A linear basis was used for EFG and standard Q4 elements were used in Ω_F. The support of the weight function d_{m_I} was computed from (3.11). Since regular arrangements of nodes were used, c_I was chosen to be equal to the distance between node I and its closest neighbor.

For convergence studies, two error norms were used. The L_2 error in displacement is computed by

$$\|E\|_2 = \left[\int_\Omega (u^h - u^{exact})^T(u^h - u^{exact})\,d\Omega\right]^{1/2}.$$ (5.4)

The energy error norm is defined by

$$\|E\|_e = \left[\int_\Omega \frac{1}{2}(\varepsilon^h - \varepsilon^{exact})^T(\sigma^h - \sigma^{exact})\,d\Omega\right]^{1/2}.$$ (5.5)

Errors in displacement and energy convergence plots are shown in Fig. 8, and the rate of convergence is indicated by the value of p. For different values of d_{max} the results were almost identical. The reason for this is the EFG has a substantially higher convergence rate and absolute accuracy than the finite elements and therefore the finite element mesh accounts for almost all of the error.

5.2
Elastodynamics

The system of equations in (4.4) is solved numerically using central difference time integration. The integrals in (4.5) are evaluated by numerical quadrature. For the following examples, the EFG domain contains a regular square grid of cells; nodes are placed at the corners of each cell.

The time step was specified according to Δt_{crit} from the Courant condition: $\Delta t_{crit} = h/c_d$, where h is a mesh characteristic parameter and c_d is the dilational wave speed in the material. The parameter h was set to the minimum distance between nodes (FE or EFG). Δt_{crit} is conservative for the EFG method [Lu, Belytschko, and Tabbara (to appear)].
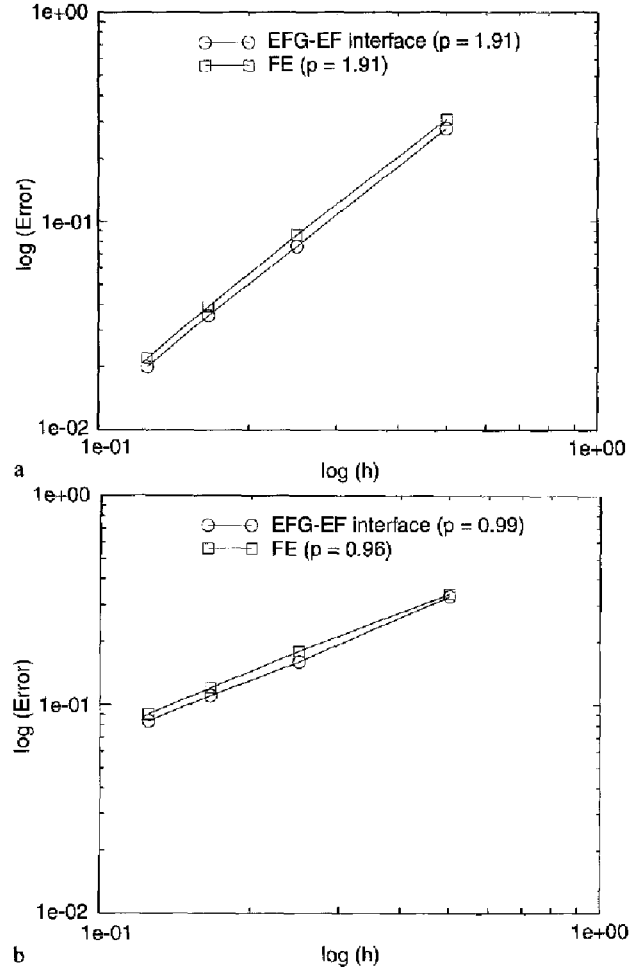
Fig. 8a-b. Convergence plots for the cantilever beam problem. Results are plotted for four meshes: 51 nodes, 155 nodes, 343 nodes, and 585 nodes. a L_2 error norm of displacement. b Energy norm

5.2.1
One dimensional wave propagation

To show the performance of the coupled method in transient problems, a one dimensional wave solution was obtained. A rod was subjected to a step traction at one end with the other end fixed (see Fig. 9 (a)). The discretization consisted of 51 nodes with an interface element placed at the midspan so that each domain, Ω_E and Ω_F, would cover almost half of the rod. The material properties and dimensions were set to unity for convenience: $E = 1.0$, $\rho = 1.0$, $l = 1.0$, and $A = 1.0$. The time step was set to half the critical, $\Delta t = \frac{1}{2}\Delta t_{crit}$, and 200 steps were run so that the wave would travel to the fixed end and back to the load point. The step load was $\sigma(t) = H(t)\sigma_0$, where $H(t)$ is the Heavyside step function and σ_0 was set to 1.0 for convenience. For the EFG shape functions, the cubic spline weight function in (3.10b) was used with $d_{max} = 2.0$.

Two simulations were run; the first with Ω_E at the load point and Ω_F at the fixed end, and the second with the domains reversed. Time plots of the velocity were generated for two points along the rod: $x = 0.3l$ and $x = 0.7l$. The exact solution for the velocity at these points is shown in Fig. 9(b,c) along with the numerical results. In separate EFG or FE simulations (not shown), both methods exhibit Gibb's
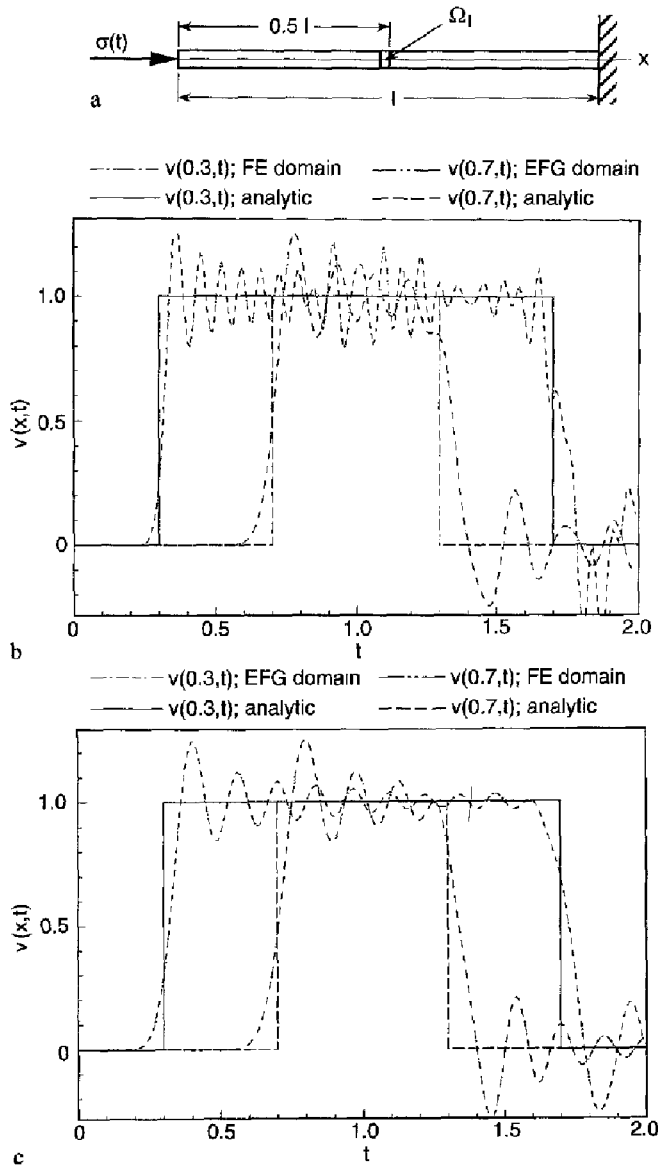
Fig. 9a–c. One dimensional wave propagation using the FE-EFG coupling. The step wave travels the length of the rod and back to the load point. a One dimensional rod configuration. b Solution with Ω_F at the load point and Ω_E at the fixed end. c Solution with Ω_E at the load point and Ω_F at the fixed end

phenomenon as expected, but the EFG solution oscillates at a lower frequency. This is typical of EFG solutions which usually exhibit smoothed results for the same number of nodes. The coupled method behaves in a manner similar to the separate methods, with some slight differences depending on the locations of the domains. When the step wave travels from Ω_F to Ω_E as in Fig. 9(b), the higher oscillations in Ω_F are reduced when the wave enters Ω_E, and there is a slight reflection due to the interface. In contrast, when the wave travels from Ω_E to Ω_F as in Fig. 9(c), there is no reflection, and the FE domain retains the frequency of oscillation exhibited by EFG. Hence, the coupling behaves as if it was completely EFG when the wave travels from Ω_E to Ω_F. Overall, the solution is only affected slightly by the interface element when compared to a solution using a single method.

5.2.2
Dynamic fracture

To model dynamic fracture numerically, the crack is placed in Ω_E, and is restricted to propagate only in this domain, since Ω_F is not able to handle arbitrary propagation directions without remeshing. The maximum hoop stress, σ_h^m, is used as a criterion for crack initiation; when σ_h^m exceeds the critical hoop stress, σ_h^c, the crack grows in a direction perpendicular to σ_h^m. The critical hoop stress is based on the dynamic fracture toughness, K_I^c, obtained from mode I experiments. Once growth is initiated, the crack is restricted to propagate at a constant velocity, unless the fracture criterion is violated, in which case crack arrest occurs. The crack tip stresses are computed from the stress intensity factors K_I and K_{II}, which are obtained using path-independent contour integrals [Nishioka and Atluri (1983), Nishioka and Atluri (1984)] that have been converted to domain form [Moran and Shih (1987), Li Shih, and Needleman (1985)]. For mixed mode conditions, the stress intensity factors are decoupled using conservation contour integrals with known auxiliary fields [Yau, Wang, and Corten (1980)]. Due to limitations in the domain integral computation, for which a straight crack segment must be of finite length in order to get reasonable accuracy in the stress intensity factors, the crack path is approximated as a series of segments. For more detail on modeling dynamic fracture using EFG, see Belytschko and Tabbara (to appear).

As a dynamic crack propagation example, we chose to simulate the brittle crack growth experiments of Kalthoff and Winkler (1987). The experimental setup, shown in Fig. 10, consists of a completely free steel plate with two parallel edge notches. A steel projectile impacts the plate between the two notches to induce in-plane shear (mode II) loading. The experimental results define 3 regimes for failure depending on strain rate, which is determined from the impact velocity and the crack tip radius. For moderate strain rate, which is simulated here, the specimen failed in a tensile fracture mode, with the crack propagating at a 70° angle from the original crack direction.

A numerical solution to this problem using EFG only can be found in Belytschko and Tabbara (to appear). Due to symmetry, only the top half of the plate is modeled in the numerical simulation. The plate dimensions are given in Fig. 10, and the material properties are for high strength maraging steel (18Ni1900) [Decker (1979)]: $E = 190 \times 10^9$ Pa, $v = 0.30$, $\rho = 8000$ kg/m^3, and $K_I^c = 68 \times 10^6$ Pa $\sqrt{\text{m}}$. The discrete model
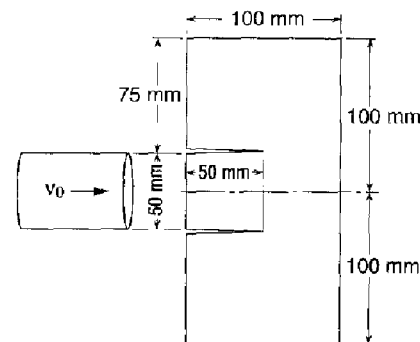
Fig. 10. Specimen for the dynamic fracture experiments performed by Kalthoff and Winkler (1987)

consists of 101 by 101 equally spaced nodes. The EFG domain Ω_E surrounds the initial crack and the expected crack path as shown by the boxes in Fig. 11. Ω_F covers the remainder of the mesh, with a single row of interface elements separating the two domains. One point quadrature was used in Ω_F, and 6×6 trapezoidal quadrature was used in Ω_E. The Gaussian weight function in (3.10a) was used to compute the EFG shape functions with $d_{max} = 2.0$. The crack speed was prescribed as a constant, $v_c = 0.15c_s$, where c_s is the shear wave speed, and the impact velocity was $v_0 = 16.5$ m/s. The time step was 1.0×10^{-7} s, which is slightly larger than half Δt_{crit}.

The overall crack path in Fig. 11 generated using the coupled method is almost identical to the crack path from EFG, although the segment angles in the coupled method tended to fluctuate more. The stress intensity factors shown in Fig. 12 also agree well. The run time for the coupled solution was half of that required for full EFG. The run time has been further reduced by dynamically allocating high quadrature only ahead of the crack in Ω_E as the simulation progresses, which reduces the run time to one tenth that of the full EFG solution.
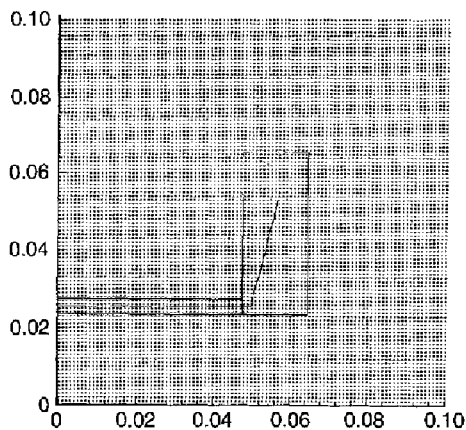

Fig. 11. Crack path after 800 steps from the numerical simulation of the experiments by Kalthoff and Winkler (1987). Each dot is a node. The boxes in the figure contain Ω_E, and the rest of the domain is modeled using FE, with a row of interface elements connecting the domains
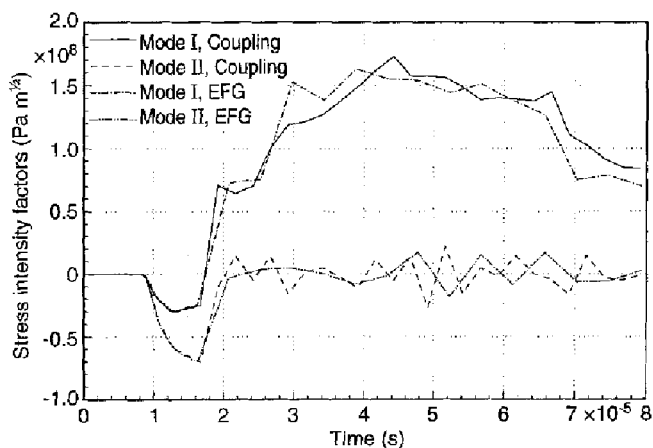

Fig. 12. Stress intensity factors from the numerical simulation of the experiments by Kalthoff and Winkler (1987). A solution from Belytschko and Tabbara (to appear) using full EFG has been included for comparison

6
Discussion and conclusions
A method for combining finite elements with meshless methods, particularly the element-free Galerkin method, has been presented. This coupling methodology provides the ability to use meshless methods in regions where finite elements become cumbersome and costly, while still maintaining the comprehensive capabilities and computational efficiency of finite element methods, since they are used in the remainder of the domain. The procedure can also be used for constructing couplings between finite elements and wavelets; see Williams and Amaratunga (1994) and Liu, Jun, Li, Adee, and Belytschko (1995). In this case, the wavelet function is represented by $\phi_I(x)$; the coupling is otherwise identical.

To establish the coupling, interface elements were defined with shape functions composed of the FE and EFG shape functions. The shape functions were constructed so that linear consistency is met exactly; consistency was also shown using the patch test with irregular meshes.

The method has been shown to perform well for elastostatic as well as elastodynamic problems. In elastostatics, even though EFG has improved accuracy, the convergence rate of the coupled method matches that of the finite element method, since it's error dominates.

In terms of computational cost, the coupled method has great advantages over a full meshless method. In the fracture example presented here, the initial savings was not overwhelming. However, although the EFG domain only covered about 8% of the full domain in that example, 75% of the integration points had to be evaluated using EFG, since more refinement was included around the crack and in the region of expected crack propagation. By dynamically adding refinement ahead of the crack as it propagated, the computational cost was reduced by a factor of 5. Computational performance is further improved in problems where the cracks are small compared to the rest of the body; the EFG subdomain is then a small percentage of the entire domain and therefore the speed of the finite elements will dictate the speed of the solution.

References
Belytschko, T.; Chang, H. S.; Lu, Y. Y. 1989: A variationally coupled finite element-boundary element method. Computers and Structures 33 (1), 17–20
Belytschko, T.; Lu, Y. Y.; Gu, L. 1994: Element-free Galerkin methods. International Journal of Numerical Methods in Engineering 37: 229–256
Belytschko, T.; Lu, Y. Y.; Gu, L.; Tabbara M. (1995). Element-free Galerkin methods for static and dynamic fracture. International Journal of Solids and Structures, Volume 32, # 17, pp 2547–2570
Belytschko, T.; Tabbara M. (to appear): Dynamic fracture using element-free Galerkin methods. International Journal of Numerical Methods in Engineering
Decker, R. F. (Ed.) 1979: Source Book on Maraging Steels. American Society for Metals
Hughes, T. J. R. 1987: The Finite Element Method. Englewood Cliffs, New Jersey: Prentice-Hall
Kalthoff, J. F.; Winkler, S. 1987: Failure mode transition at high rates of shear loading. In C. Y. Chiem, H. D. Kunze, and L. W. Meyer (Eds.), International Conference on Impact Loading and Dynamic Behavior of Materials, Volume 1, pp. 185–195
Lancaster, P.; Salkauskas, K. 1981: Surfaces generated by moving least squares methods. Mathematics of Computation 37: 141–158

Lancaster, P.; Salkauskas, K. 1986: Curve and Surface Fitting. Academic Press

Li, F. Z.; Shih, C. F.; Needleman, A. 1985: A comparison of methods for calculating energy release rates. Engineering Fracture Mechanics 21 (2): 405–421

Liu, W. K.; Jun, S.; Li, S.; Adee, J.; Belytschko, T. 1995: Reproducing kernel particle methods for structural dynamics. International Journal for Numerical Methods in Engineering 38: 1655–1679

Lu, Y. Y.; Belytschko, T.; Gu L. 1994: A new implementation of the element free Galerkin method. Computer Methods in Applied Mechanics and Engineering 113: 397–414

Lu, Y. Y.; Belytschko, T.; Liu, W. K. 1991: A variationally coupled FE-BE method for elasticity and fracture mechanics. Computer Methods in Applied Mechanics and Engineering 85: 21–37

Lu, Y. Y.; Belytschko, T.; Tabbara, M. (to appear): Element-free Galerkin methods for wave propagation and dynamic fracture. Computer Methods in Applied Mechanics and Engineering

Moran, B.; Shih, C. F. 1987: Crack tip and associated domain integrals from momentum and energy balance. Engineering Fracture Mechanics 27 (6): 615–641

Nayroles, B.; Touzot, G.; Villon, P. 1992: Generalizing the finite element method: diffuse approximation and diffuse elements. Computational Mechanics 10: 307–318

Nishioka, T.; Atluri, S. N. 1983: A numerical study of the use of path independent integrals in elasto-dynamic crack propagation. Engineering Fracture Mechanics 18 (1): 23–33

Nishioka, T.; Atluri, S. N. 1984: On the computation of mixed mode K-factors for a dynamical propagating crack, using path-indpendent integrals J_k'. Engineering Fracture Mechanics 20 (2): 193–208

Nishioka, T.; Atluri, S. N. 1986: Computational methods in dynamic fracture. In S. N. Atluri, (Ed.), Computational Method in the Mechanics of Fracture, Chapter 10, pp. 336–383. Elsevier

Timoshenko, S. P.; Goodier, J. N. 1970: Theory of Elasticity (Third ed.). New York: McGraw Hill

Williams, J. R.; Amaratunga, K. 1994: Introduction to wavelets in engineering. International Journal for Numerical Methods in Engineering 37: 2365–2388

Yau, J. F.; Wang, S. S.; Corten, H. T. 1980: A mixed-mode crack analysis of isotropic solids using conservation laws of elasticity. Journal of Applied Mechanics 47: 335–341